DOI: 10.6119/JMST-016-0115-2

OPTIMAL DESIDN OPERATION PARAMETERS ON PERFORMANCE OF PEMFC

Ying-Pin Chang

Key words: neural-network, orthogonal arrays, response surface methodology, PEMFC, operation parameters.

ABSTRACT

This paper presents a method for combining sequential neural-network approximation and orthogonal arrays (SNAOA) in determining the operation parameters on the performance of the proton exchange membrane fuel cell (PEMFC). An orthogonal array was first conducted to obtain the initial solution set. The results obtained from the orthogonal array were then used as the experimental data for response surface methodology (RSM) that could predict the operation parameters at discrete levels. The set was then treated as the initial training sample. Next, a back-propagation sequential neural network was trained to simulate the feasible domain for seeking optimal operation parameters of PEMFC. The size of the training sample was greatly reduced due to the use of the orthogonal array. In addition, a restart strategy was also incorporated into the SNAOA so that the searching process may have a better opportunity to reach a near global optimum. The objective is to maximize the output power of the PEMFC. The results show that, the uniform cell reaction was achieved using the split flow field in a PEMFC at different temperatures and flow ratios. The prediction model of major operation parameters influencing the performance of a PEMFC with a split flow field was also developed using the SNAOA. The optimal parameters were an operating temperature of 78^{o}C, an anode humidification temperature of 72^{o}C, an anode flow rate of 296sccm, a cathode flow rate of 295sccm, a split flow rate of 145sccm and a split point 44%.

I. INTRODUCTION

A fuel cell (FC) is a device that converts the chemical energy from a fuel into electricity through a chemical reaction with oxygen as the oxidizing agent. Hydrogen is the most common fuel, but hydrocarbons such as natural gas and alcohols such as methanol are sometimes used. FCs are different from batteries in that they require a constant source of fuel and oxygen to run, but they can produce electricity continuously as long as these inputs are supplied. In the efficient frontier design of the archetypical hydrogen-oxygen performance of proton exchange membrane fuel cell (PEMFC), a proton-conducting polymer membrane, the electrolyte, separates the anode and cathode sides. In a PEMFC stack, the cells are electrically connected in series and the polarization curves of the individual cells can be obtained by measuring the current of the entire stack and the voltages of individual cells (Lee et al., 2011).

In a PEMFC stack, the cells are electrically connected in series and the polarization curves of the individual cells can be obtained by measuring the current of the entire stack and the voltages of individual cells. For a given set of operating parameters such as pressure, temperature, humidification, and gas stoichiometry, the voltage of the fuel cell is essentially determined by the applied current (Ibrahim and Li 2012; Buxbaum and Lei 2003; Cho et al., 2008; Janssen and Overvelde 2001; Low and Hung 2009; Tsain 2012). The Nexa power module is evaluated at membrane-electrode-assembly (MEA) and stack levels. The Nexa PEMFC system is measured by periodic current interruption to maintain isothermal stack temperature. The uniformity analysis was mainly performed on the load of 800W for all MEAs in Nexa (Rodatz et al., 2004). Hydrogen for a current polymer electronic membrane (PEM) and an alkaline FC must be supplied no more than a few tens of ppm of CO or CO2, respectively. If the hydrogen is generated, as it is used, it must be produced efficiently over a broad FC demand range, and follow load changes on the order of seconds. This paper generated hydrogen for a broad variety of demands from 1.09/l molar mix of methanol/water using a commercial water-gas shift catalyst and a membrane reactor (Buxbaum and Lei 2003). Catalyst layers for PEMFC were prepared by spraying and sputtering to deposit Pt amount of 0.1 and 0.01 mg cm-2, respectively (Cho et al., 2008). These Pt layers were then assembled to fabricate MEA having either single- or double-layered catalysts. These results indicate that Pt loading in state-of-the-art PEMFCs could be reduced by approximately 50% with no performance loss using both spraying and sputtering method in the MEA fabrication process. The water transported in PEMFCs has been experimentally investigated by measurements of the effective or net drag coefficient. Results were presented in a wide range of operating conditions as well as for different types of membrane-electrode-assemblies (Janssen and Overvelde 2001). Yoon et al., (2003) presented

Author for correspondence: Ying-Pin-Chang (e-mail:cyp@nkut.edu.tw). Department of Electrical and Information Engineering, Nan Kai University of Technology, Nantou, Taiwan , R.O.C.

DOI: 10.6119/JMST-016-0115-2

the current and temperature distributions along with the variation of gas compositions in the cell of PEMFC which are crucial for designing cell components, such as the flow field plate and the membrane-electrode assembly. The influences of flooding and stoichiometry variation of the feed gas were discussed in the rate of electrochemical reaction from the measured distributions of local currents in a segmented single cell. Janssen and Overvelde (2001) proposed the spatial current density distributions in a single PEMFC with three serpentine flow channels. It was measured using a segmented bipolar plate and printed circuit board technique. The effects of key operating conditions such as stoichiometry ratios, inlet humidity levels, cell pressure and temperature on the local current density distributions for co-, counter-, and cross-flow arrangements were examined.

Recently, some of the methods used to estimate the output voltage of proton exchange membrane fuel cell (PEMFC) accurately combined evolutionary algorithms (EAs), neural networks (GANN) model, response surface methodology (RSM) and the Taguchi method. (Chang 2011; Hattia and Tioursic, 2011; Dong'an et al., 2007; Li et al., 2011; Yoon et al., 2003; Chang et al., 2009). Dong'an et al., (2007) presented a robust design analysis based on RSM. The analysis was performed on a simplified fuel cell stack in order to identify the effect of assembly parameters on MEA pressure distribution. The assembly pressure and bolt position were considered as randomly varying parameters with probabilistic properties and acted as the design variables. Combining the genetic algorithm neural network (GANN) model and the Taguchi method was adopted for estimating the output voltage of PEMFC (Chang, 2011). Li et al., (2011) presented an electrochemical-based PEMFC mechanism model which was suitable for engineering optimization and adaptive particle swarm optimization. Hattia and Tioursic (2011) also dealt with the control and management of a hybrid PV/PEMFC energy system, using Matlab/Simulink, optimizing the hybrid system devices using artificial intelligence and carry out simulation studies using a real climate data and practical load profile . A new approach to estimate the optimal performance of an unknown PEMFC was proposed. This proposed approach combines the Taguchi method and the numerical PEMFC model. Experimental results on the test equipment showed that the proposed approach was effective in optimal performance estimation for the tested unknown PEMFC, thus demonstrating the success achieved by combining the Taguchi method and the numerical PEMFC model (Chang et al., 2009). This paper presented a new approach to estimate the output voltage of PEMFC accurately by combining the use of a back-propagation neural network (BPNN) model and the Taguchi method. Finally, this approach has estimated the values of output voltage of PEMFC from BPNN model without using Taguchi method (Chang and Teng, 2012).

A sliding-level orthogonal differential evolution algorithm with a two-level orthogonal array (SLODEA2OA) is proposed for solving worst-case tolerance design problems. Tolerance affects system performance and leads to violation of design constraints. By including a two-level orthogonal array, the proposed SLODEA2OA obtains robust optimal solutions that minimize the impact of parameter variations and maintain compliance with a comprehensive constraint set (Tsain, 2012).

This report also presented a method of combining sequential neural network approximation and orthogonal arrays (SNAOA) for the planning of large-scale harmonic filters (Chang et al., 2007).

The planning of operation parameters on the performance of PEMFC with discrete variable in the power system belongs to the constrained combinatorial optimization problems. Such planning is difficult to solve by conventional methods, such as exhaustive search (Dong'an et al., 2007). Owing to the ANN's excellent ability in dealing with the combinatorial optimization problems and the merit of orthogonal arrays that can systemically reduce the number of trails in the experimental process, in this study, an SNAOA is adopted to find the optimal design of discrete-value operation parameters on PEMFC. The UWA communication channel is generally considered as an unfavorable and difficult environment for data transmission. Its multipath fading and Doppler spreading effects make the building of a reliable UWA communication system a challenging task. Most commercially available UWA communication systems developed so far use noncoherent modulation schemes like the frequency shift keying (FSK) for simplicity. However, as the hardware technology progresses, the focus of the UWA communication research has been shifted toward more complicated coherent modulation schemes such as phase shift keying (PSK) and quadrature amplitude modulation (QAM) (Stojanovic, 1996; Kilfoyle and Baggeroer, 2000). Furthermore, the design of UWA transceivers has been revolutionized over the past few years due to the tremendous advances in DSP technology (Labat, 1994; Trubuil et al., 2001; Choi et al., 2003b; Yagnamurthy and Jelinek, 2003). The digital VLSI offers communication engineers a platform to realize algorithms that were frequently inconceivable in the analog domain. Specifically, Choi et al. (2003a, 2003b) presented a design of phase-coherent all-digital UWA transceiver whose frame synchronization method requires neither a phase-locked loop (PLL) nor a delay-locked loop (DLL), and the operation of the transceiver relies largely on the adaptive equalizer and the Viterbi decoding algorithm. Trubuil et al. (2001) developed a real-time high data rate UWA communication link, where a self-optimized configuration multiple input decision feedback equalizer (SOC-MI-DFE) was proposed and implemented on a TMS320 C6201 DSP module. These all-digital implementations require the sampling of the received signal to be synchronized to the incoming symbols. Interpolation methods for achieving such synchronization have also been proposed by several researchers (Vesma and Saramaki, 1996; Lu et al., 2004).

II. MODELING AND OPTIMIZATION APPROACH

1. Sequential approximation method

(1). Model representation

A combinatorial optimization problem can be formulated as

$$\text{Maximum } M(\underline{X})$$

DOI: 10.6119/JMST-016-0115-2

subjected to

$$g_j(\underline{X}) \le 0,\ j = 1,...,n_g$$
$$g_b(\underline{X}) = 1,\ b = 1,...,n_b \quad (1)$$

where $M(\underline{X})$: objective function of discrete variable vector $\underline{X}$, and $\underline{X} = \left[X_1, X_2, .., X_j, .., X_D\right]^t$. Each element of $\underline{X}$ belongs to an individual solution set, i.e., $X_i \in \left\{X_{i,1}, X_{i,2}, X_{i,3}, \cdots, X_{i,mD}\right\} \quad \forall i = 1,2,3,\cdots,D$

$g_j(\underline{X})$: inequality constraint

$g_b(\underline{X})$: "pass-fail" binary constraints

The feasible domain of the optimization model in (1) can be simulated using a few representative data to form the approximated model as

Maximum $M(\underline{X})$

subjected to

$$NN(\underline{X}) = 1 \quad (2)$$

where the binary constraint $NN(\underline{X}) = 1$ approximates the feasible domain. If $NN(\underline{X}) = 1$, the discrete point $\underline{X}$ is feasible; and if $NN(\underline{X}) = 0$, the discrete point $\underline{X}$ is infeasible. The discrete variable constraints are embedded in the format of the input nodes of the neural network. Throughout this report, the optimization model will be denoted as M_{real}, and the approximate model will be denoted as M_{NN}.

(2). Structure of proposed method

The basic idea of sequential approximation methods is to use a simple sub-problem to approximate the hard and exact problem. In this method, to predict the relationship between the pertinent variables and the objective function, some experiments have first been designed through orthogonal arrays, since this procedure can systematically reduce the number of experiments required. A back-propagation neural network is then applied to search for the optimum design of a tilt angle for modules. In the training process, sequential neural-network approximation (SNA) is trained to simulate a rough map of the feasible domain formed by the constraints using a few representative training data. In the searching process, when a new design point is obtained which has a better performance with respect to the corresponding objectives, the point is checked against the true constraints to see whether it is feasible, and is then added to the training set. The neural network is then trained again with this added information to have a better simulation for the boundary of the feasible domain of the true optimization problem; thus the searching process continues to seek other "new design points" with this new approximate feasible domain as well. These processes continue in an iterative manner until the approximate model insists on the same design point in consecutive iterations.

Figure 1 outlines the sequential approximation method using neural networks. The initial training data $\{\underline{X}^0\}$, with at least one feasible point was given. A back-propagation neural network was trained to simulate a rough map of the feasible domain to form the initial optimization model M_{NN}. Starting from the lowest objective value $\underline{X}_b^0$ among the feasible solutions, a search algorithm was used to search for the solution $\underline{X}_b^G$ of M_{NN} in the G-th iteration. This solution $\underline{X}_b^G$ is then evaluated to determine whether it is feasible in M_{real}, and whether $\underline{X}_b^G = \underline{X}_b^{G-1}$. If not, this new solution point $\underline{X}_b^G$ is added to the training solution $\{\underline{X}\}$, and the neural network is trained again with the updated data solution. Then a search is begun for the solution in the updated M_{NN} again by using $\underline{X}_b^G$ as the starting solution if $\underline{X}_b^G$ is feasible. With an increasing number of training solutions, it is expected that the feasible domain simulated by the neural network in M_{NN} will approach that of the exact model M_{real}.

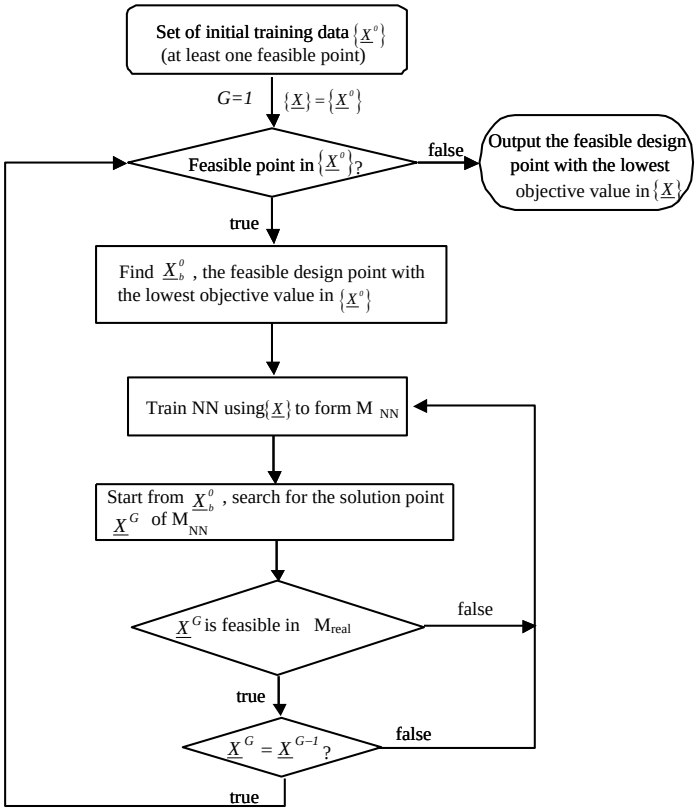

Fig. 1. Flow chart of algorithm

(3). Training neural network

Figure 2 shows the architecture of the three-layer network. Each neuron in the input layer had a value of 1 or 0 to represent the discrete value corresponding to each variable. There was only a single neuron in the output layer to represent the feasibility or infeasibility of this design point. The number of neurons in the hidden layer depends on the number of variables in the input layer. The transfer functions used in the hidden and output layer of the network were log-sigmoid functions. The value of the neuron in the output layer had a range of [0,1]. According to Chang et al. (2007) and Low et al. (2009), as the threshold of the neuron was set to 0.25, operation parameters of PEMFC was meaningful on output voltage. After the training was completed, the threshold of 0.25 was applied to the output layer in the boundary of the feasible domain. In other words, when given a discrete design point in the search domain, the

DOI: 10.6119/JMST-016-0115-2

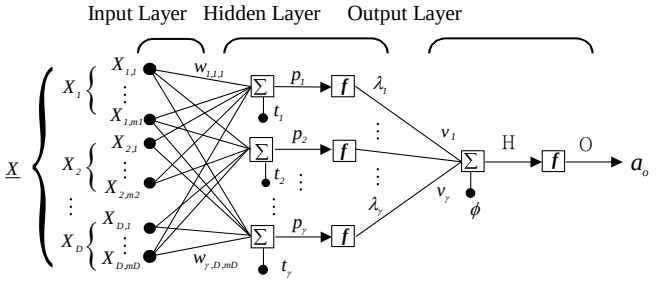

$\underline{X}$ = input variable vector ϕ, t = bias, w, v = weight γ = number of neuron in hidden layer, f = transfer function, a_0 = output neuron, D = number of dimension

Fig. 2. Architecture of neural network

network always output 0 or 1, which indicated feasibility or infeasibility of the design point.

(4). Searching in feasible domain

Figure 3 shows the flow chart of this discrete search algorithm, which begins from a feasible design point. If a new design solution from the previous iteration was feasible in M_{real}, it was used as the next solution in the current search. If a new design solution was infeasible in M_{real}, the other solution used in the previous iteration was used again in the current search. As discussed earlier, there must be at least one feasible design point in the solution of initial training points in order that the algorithm can execute from a feasible design solution.

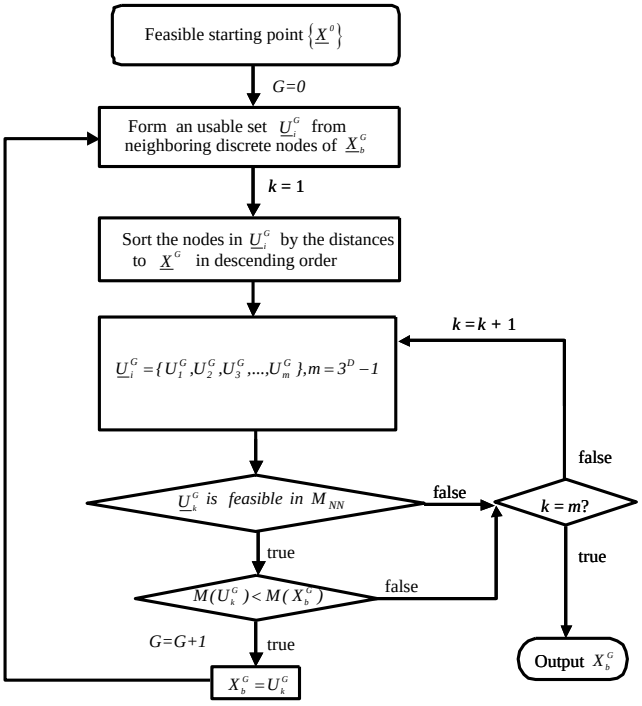

Fig. 3. Flowchart of search steps

(5). Restart strategy

To ensure that a solution had a better chance to reach an optimum in the searching process, the searching process was restarted from another feasible point in $\{\underline{X}^0\}$, which had the second lowest objective value. The searching process was terminated when either all points in $\{\underline{X}^0\}$ was feasible or the same design point was obtained in two consecutive iterations. Finally, the feasible design point with the lowest objective value in $\{\underline{X}\}$ was the optimum solution.

(6). Orthogonal arrays

The primary advantage of t orthogonal arrays is to enhance realization of the characteristics of the parameters. For a given set of variables, all states of other variables should exist by an equal number of times. This situation constituted a balanced experiment and permitted the objective function of one variable under study to be separable from the objective function of other variables. The result was that the findings of the experiment were reproducible. An additional advantage of orthogonal arrays was efficiency. Although balanced, the design of orthogonal arrays did not require that all combinations were tested. Therefore, the experimental matrix can be reduced without losing any vital information.

Table 1 shows an $L_{27}(3^6)$ orthogonal array that can deal with four variables in three states under nine experimental conditions. "Orthogonal" means to balance and not to mix.. In the context of experimental matrices, the term means statistically independent. From Table 1, it can be easily observed that each state had an equal number of manifestations within each column. Concerning about statistical independence, this idea of balance goes farther than meaning simply an equal number of variables within each column.

Table 1 $L_{27}(3^6)$ orthogonal array

Exp.	X_1	X_2	X_3	X_4	X_5	X_6
1	1	1	1	1	1	1
2	1	1	1	1	2	2
3	1	1	1	1	3	3
4	1	2	2	2	1	1
5	1	2	2	2	2	2
6	1	2	2	2	3	3
7	1	3	3	3	1	1
8	1	3	3	3	2	2
9	1	3	3	3	3	3
10	2	1	2	3	1	2
11	2	1	2	3	2	3
12	2	1	2	3	3	1
13	2	2	3	1	1	2
14	2	2	3	1	2	3
15	2	2	3	1	3	1
16	2	3	1	2	1	2
17	2	3	1	2	2	3
18	2	3	1	2	3	1
19	3	1	3	2	1	3
20	3	1	3	2	2	1
21	3	1	3	2	3	2
22	3	2	1	3	1	3
23	3	2	1	3	2	1
24	3	2	1	3	3	2
25	3	3	2	1	1	3
26	3	3	2	1	2	1
27	3	3	2	1	3	2

2. Response Surface Methodology

Response Surface Methodology (RSM), a collection of mathematical and statistical technique, is useful for developing, improving, and optimizing processes; and it can be used to evaluate the relative significance of several affecting factors even in the presence of complex interactions. Applications of

DOI: 10.6119/JMST-016-0115-2

RSM can be found in chemical, engineering and clinical sciences. Nevertheless, it does not seem to be an established code of practice for the automated application of RSM in the field of simulation optimization (Dong'an et al., 2007).

A second-order model is commonly used for the multidisciplinary design in RSM. In general, the response model can be expressed as follows:

$$Y = \beta_o + \sum_{i=1}^{k} \beta_i X_i + \sum_{i=1}^{k} \beta_{ii} X_i^2 + \sum \sum_{i<j} \beta_{ij} X_i X_j + \varepsilon \quad (3)$$

where Y is the response variable, X is the independent variable, ε is the reaction of the observed noise or error, and $\beta_o, \beta_i, \beta_{ii}, \beta_{ij}$ are coefficients of the second-order regression equation. Figure 4 show experimental flowchart using RSM.

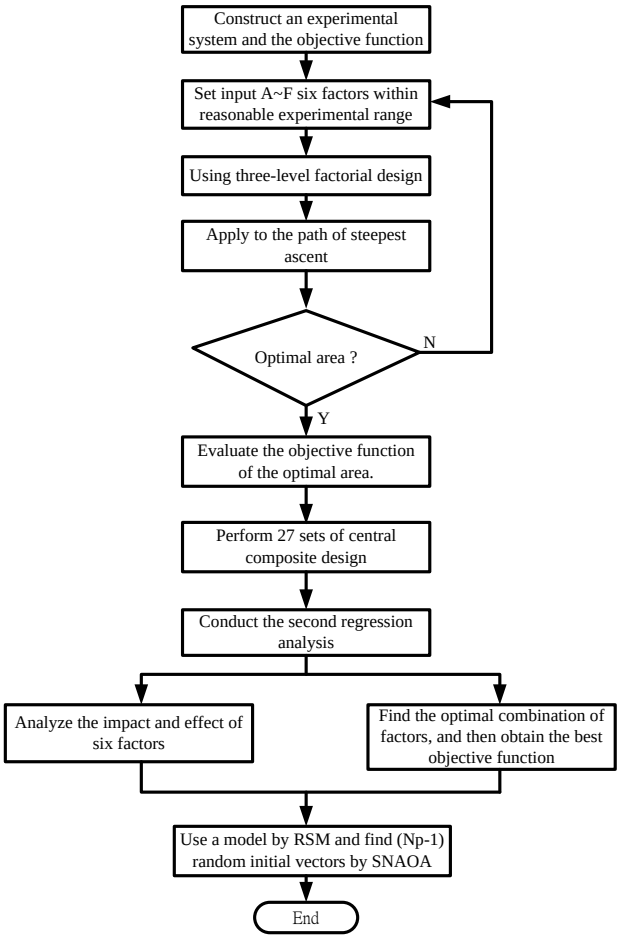

Fig. 4. Experimental flowchart using RSM

III. SYSTEM UNDER STUDY

Figure 5 shows the operating principle of PEMFC. Proton exchange membrane was used as a single cell fuel cell, of which the structure was divided into seven layers in the experiments. The observation sequence are as follows: first the anode terminal, then the anode gas flow channel, the anode gas diffusion layer and the anode catalyst layer, the proton exchange membrane, the cathode catalyst layer, the cathode gas diffusion layer and the cathode gas flow channel. Usually, a five-layer membrane electrode assembly MEA includes an anode gas diffusion layer order anode catalyst layer, proton exchange membrane, the cathode catalyst layer and the cathode gas diffusion layer.

Performance test equipment of PEMFC was used in this study; its control module includes the following five components: temperature and humidifier control modules, gas supply equipment, electronic load, and flow control system, as shown in Figure 6. The experiment was conducted on a test platform manufactured by the Beam Associate Co., Ltd. Electrical parameters were as follows: the maximum power is 600W; maximum current upper limit is 80A and maximum voltage upper limit is 8V. Test gas is hydrogen in anode; the cathode contains two different gases: oxygen and air. This set of experimental test platform was suitable for fuel single battery and fuel cell stack. The major components of test platform were as follows: the supply of in reaction gases, gas humidifier and sensors, temperature control modules for battery and the electronic load system. Test platform also connected to a computer and the test data will be stored into the computers through the connection transmission system.

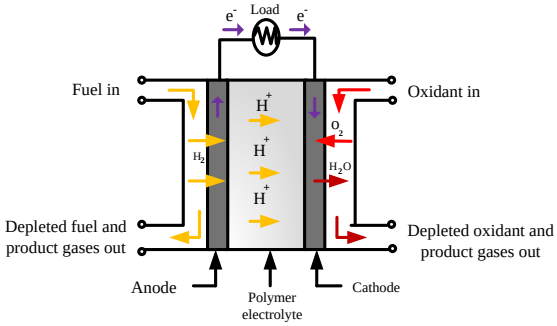

Fig. 5. PEMFC principle

Fig. 6. Performance test equipment of PEMFC

Bipolar plate in an FC stack that acts as an anode for one cell and a cathode for the adjacent cell is shown in Figure 7. The plate may be made of metal or conductive polymer which may be a carbon-filled composite. The plate usually incorporates flow channels for the fluid feeds and may also contain conduits for heat transfer. The thickness of the graphite will affect FC performance. If it is too thin, it will be easily broken. On the contrary, if it is too thick, it will reduce performance. Therefore, the thickness of plate should be selected properly. Figure 8 shows an FC flow channel plate with gas holes. The plates used in this study had an additional gas hole in the flow channel plate of the fuel. Therefore, the flow channel of the bipolar panel opens another hole to allow flowing not only from the inlet port for the reaction gas, but also from the middle of the channel

DOI: 10.6119/JMST-016-0115-2

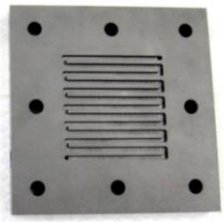

Fig. 7. Bipolar plate in a FC

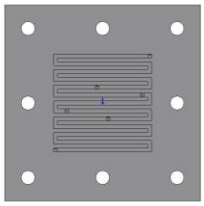

Fig. 8. FC flow channel plate with gas hole

input. It reduces the concentration variation of the reaction gas at different locations, improve the performance of the reaction discharge.

IV. OPTIMAL DESIGN OF OPERATION PARAMETERS ON PEMFC

PEMFC possesses the merits of high efficiency of energy conversion, low operating temperature, and no pollution. It uses a solid polymer membrane as the electrolyte for cell reaction, and the ions conductivity were enhanced through the control of proper operation temperature and humidification. As the output current increases during reaction of FC, the concentration polarization phenomenon emerges around downstream region of the channel, and it expands gradually toward upstream. This phenomenon is obvious when the reactant flow rate is insufficient. It causes a serious non-uniform distribution of reaction and deteriorates overall cell performance. In this study, a cathode flow field was designed with an additional port as inlet split point. Besides the original inlet port, the reactant gas was supplied from this split point in order to reduce the maldistribution of reactant and product concentration. The effects of the split point position and split flow rate on the polarization curve was discussed and compared with those of traditional flow fields at various operating conditions.

This study through the experiments at different temperature and flow ratio setting, the uniform cell reaction is achieved using the split flow field in PEMFC. The prediction model of major operation parameters influencing the performance of PEMFC with a split flow field is also developed on using SNAOA.

1. Objective function

The objective of this study was to implement an design for operation parameters on PEMFC so that the output power can be significantly increased. The constraints of the operation parameters were also considered. The calculation of operation parameters on PEMFC can be formulated as a combinatorial optimization problem as follows:

$$\text{Maximum } M(\underline{X}) = \text{Maximum } M(X_1, X_2, X_3, X_4, X_5, X_6) = P_o \quad (4)$$

Where M: objective function for six factor operation parameters on the PEMFC, and X_1, X_2, X_3, X_4, X_5 and X_6 denotes the six operation parameters on the PEMFC, and P_o represents the output power of the PEMFC. Table 2 lists that operation parameters on the PEMFC and the level values.

2. Constraints

(1) Limits of the six factors of operation parameters

$$X_{1\sim6}^{\max} > X_{1\sim6} > X_{1\sim6}^{\min} \quad (5)$$

Table 2 Operation parameters on the PEMFC and their level values

Factor	Parameter	Level 1	Level 2	Level 3
X_1	FC temperature (℃)	50	65	80
X_2	FC humidification temperature (℃)	55	70	85
X_3	anode stoichiometry flow rate (sccm)	200	250	300
X_4	cathode stoichiometry flow rate (sccm)	200	250	300
X_5	cathode split flow rate (sccm)	50	100	150
X_6	location of the split (%)	35	45	55

where $X_{1\sim6}^{\max}$ and $X_{1\sim6}^{\min}$ are the upper and lower bound of the six operation parameters on the PEMFC.

V. RESULTS AND DISCUSSION

The response surface plot of simulation result is shown in Figure 9. Figure 9(a) shows the residual plot of this method. It was used to detect the normal probability. Y axis represented the percentage and x axis was the residual. The value of y axis ranged from 99% to 1% while the distribution of the residual was between +0.4 and -0.4. A straight line of y=196x+50 with a variation of R^2=0.98was obtained, indicating the characteristic of normal distribution. The histogram of the residual values is plotted in Figure 9(b). It was used to detect the several peaks, outliers and non-normality. The random variation frequency was at the range of 0-34 with the maximum value of 34 for residual 0. It was also shown that the residual was about 10 at the frequencies of ±0.01, and was 1 at ±0.02 and ±0.03. Therefore, it was close to the bell-shaped and represented the normal distribution. Figure 9 (c) shows the residual fit, which is to detect non-uniform variance peak and missing higher-order terms with outliers. The Y-axis was represented by residual value, and the X axis as the FC output power. The range of out power were 11W ~ 22W in the random changes. When the residual value was zero, out power had maximum and smallest simultaneously. The resulting residuals should be randomly distributed in the range of ± 0.5. Figure 9(d) also shows the residual line chart which is to detect the time-dependence of residuals. Y axis is represented by residuals value, and X-axis is represented by the observation order.

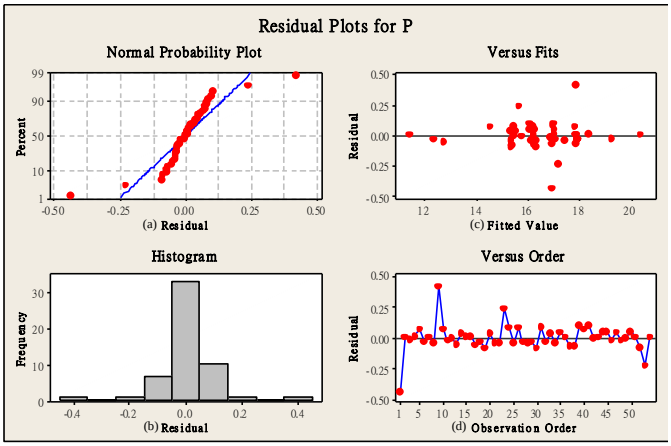

(a) linear plot (b) frequency histogram (c) residual of fits scatter plot (d) the residual line chart

Fig. 9. Statistical analysis of split flow design using RSM on PEMFC

DOI: 10.6119/JMST-016-0115-2

1. Defining set of initial training data using three-level orthogonal arrays

In this study, there were 6 design variables, each with 31 discrete values. Thus, a total of 6×31 neurons were used in the input layer. Each neuron in the input layer was a value of 1 or 0 to represent the discrete value corresponding to each variable. There was only a single neuron in the output layer to represent the feasibility or infeasibility of this design point. The number of neurons in the hidden layer depends on the number of neurons in the input layer. There were 12 neurons in the hidden layer in this practical case. The transfer functions used in the hidden and output layer of the network were log-sigmoid functions. The neuron in the output layer was a value range of [0, 1]. After the training was completed, a threshold value was applied to the output layer. In other words, for a given discrete design point in the search domain, the network always outputs 0 or 1 to indicate the feasibility or infeasibility of the point.

This training points are shown in Figure 10, where an empty circle represents a "0" in the node, and a black circle represents a "1." For illustrative purposes, the 186 input nodes were arranged in six rows to represent six design variables. The first twenty-eight nodes of the first row had a value of 1, which the first variable X_1 had the discrete value 77. The first 17 nodes of the second row with value 1 meant that the second variable X_2 also had the discrete value 71. The first 31 nodes of the third row with value 1 meant that the third variable X_3 also had the discrete value 300. The first one nodes of the fourth row with value 1 meant that the fourth variable X_4 also had the discrete value 200. The first 31 nodes of the fifth row with value 1 represented that the fifth variable X_5 also had the discrete value 150. The first 3 nodes of the sixth row with value 1 meant that the sixth variable X_6 also had the discrete value 36. By checking with, one can determine that [X_1, X_2, X_3, X_4, X_5, X_6]= [77, 71, 300, 200,150, 36] was an infeasible design point. Hence, the single node in the output layer had the value of 1, which meant that this point was infeasible. Similarly, Figure 11 shows another initial training point [X_1, X_2, X_3, X_4, X_5, X_6]= [65, 70, 300, 200,100, 55], which was a feasible design point. There was at least one feasible design point in the set of initial training points, since the search algorithm described later, had to start from a feasible design point.

For this study, the $L_{27}(3^6)$ array was used. Table 3 shows the arrangement of orthogonal arrays. The three levels were determined by both end points and one middle point of each variable within the design domain. Therefore the twenty-eight initial training points in this study are shown Table 3. Among these points, [65, 70, 300, 200, 100, 55] for starting point and [80, 70, 200, 300, 100, 35] for restart point were feasible to start the search optimum values.

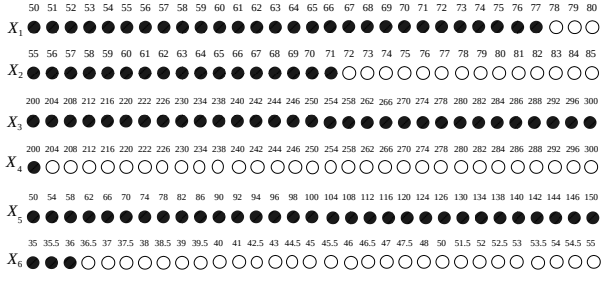

Fig. 10. Representation of an infeasible training point [77, 71, 300, 200,150, 36]

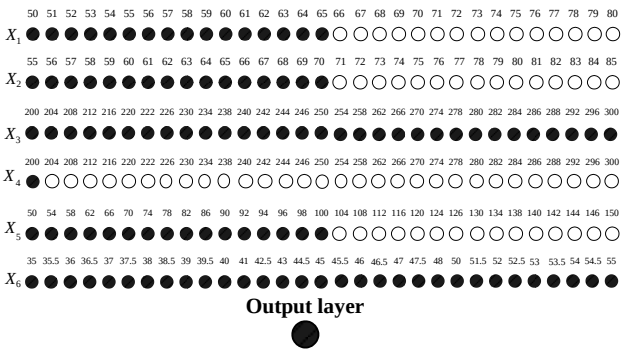

Fig. 11. Representation of a feasible training point [65, 70, 300, 200,100, 55]

Table 3 Arrangement of orthogonal arrays

Exp.	X_1	X_2	X_3	X_4	X_5	X_6
1	50	55	200	200	50	35
2	50	55	200	200	100	45
3	50	55	200	200	150	55
4	50	70	250	250	50	35
5	50	70	250	250	100	45
6	50	70	250	250	150	55
7	50	85	300	300	50	35
8	50	85	300	300	100	45
9	50	85	300	300	150	55
10	65	55	250	300	50	45
11	65	55	250	300	100	55
12	65	55	250	300	150	35
13	65	70	300	200	50	45
14	65	70	300	200	100	55
15	65	70	300	200	150	35
16	65	85	200	250	50	45
17	65	85	200	250	100	55
18	65	85	200	250	150	35
19	80	55	300	250	50	55
20	80	55	300	250	100	35
21	80	55	300	250	150	45
22	80	70	200	300	50	55
23	80	70	200	300	100	35
24	80	70	200	300	150	45
25	80	85	250	200	50	55
26	80	85	250	200	100	35
27	80	85	250	200	150	45

2. Iteration history of study

This algorithm was used to search for the solution point by the L_9 initial training points. There were two feasible design points [65, 70, 300, 200, 100, 55] and [80, 70, 200, 300, 100, 35] in the set of twenty-seven initial training points. The feasible design point [65, 70, 300, 200, 100, 55] had a lower objective value and was first used as the starting point in the search algorithm.

Figure 12 shows the iteration history of the study, in which the points represented by black circles are the feasible design points. Table 4 also shows iteration history of operation parameters form "a" start point to "h" optimum point. The search algorithm was started from "a" point [65, 70, 300, 200, 100, 55] at an objective value of 18.7W to "g" point [78, 72, 296, 295,

DOI: 10.6119/JMST-016-0115-2

145, 44] at an objective value of 24W. This search path proceeded from "a" point [65, 70, 300, 200, 100, 55], through "b" point [77, 71, 300, 200, 150, 36], "c" point [75, 71, 300, 200, 140, 35], "d" point [80, 71, 300, 200, 150, 35], "e" point [76, 70, 295, 204, 146, 45], "f" point [50, 70, 250, 250, 150, 55] and "g" point [78, 72, 296, 295, 145, 44].To ensure that a better chance for reaching a near global optimum, this search process was restarted from another feasible "g_1" point [80, 70, 200, 300, 100, 35] in the set of initial training data. In this study, the search process terminated at the same feasible point [78, 72, 296, 295, 145, 44] in one iteration. Note that a total of 34 points from the 31×31=961 possible combinatorial combinations at an objective value of 24W were evaluated to obtain this optimum design. No gradient calculation was required.

In order to demonstrate the effectiveness of the proposed method, a comparison between Taguchi method, RSM and SNAOA, is given in Table 5 (Chang et al., 2014). The results showed that Taguchi method, RSM and SNAOA had an output value of 19.05W, 21.57W and 24 W, respectively. It was found that SNAOA had greater output voltage than Taguchi method and RSM.

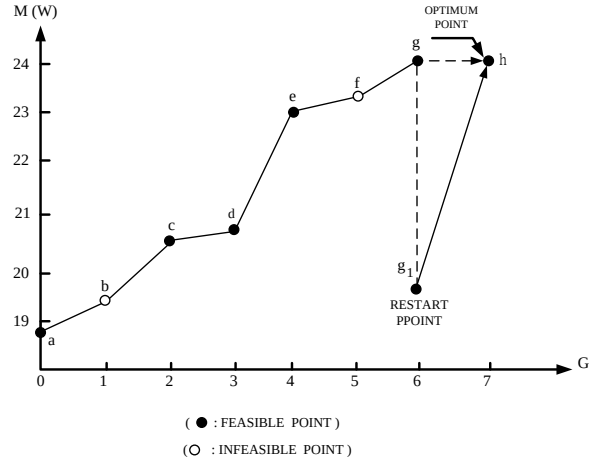

Fig. 12. Iteration history of study

Table 4 Iteration history of operation parameters

Point	X_1	X_2	X_3	X_4	X_5	X_6	P_o(W)
a	65	70	300	200	100	55	18.7
b	77	71	300	200	150	36	19.5
c	75	71	300	200	140	35	20.6
d	80	71	300	200	150	35	20.7
e	76	70	295	204	146	45	23.1
f	50	70	250	250	150	55	23.3
g	78	72	296	295	145	44	24.0
g_1	80	70	200	300	100	35	19.6
h	78	72	296	295	145	44	24.0

Table 5 A comparison of the operation parameters between Taguchi method, RSM and SNAOA

Factors	Methods		
	Taguchi method	RSM	SNAOA
A (^{o}C)	70	59.98	78
B (^{o}C)	85	68.92	72
C (sccm)	250	255.37	296
D (sccm)	300	309.15	295
E (sccm)	50	70.96	145
F (%)	55	33.17	44
P (W)	19.05	21.57	24

VI. CONCLUSION

This study has presented a combination method of SNAOA and RSM for determining discrete-value operation parameters on performance of PEMFC. Orthogonal arrays have been employed to obtain the local optimum solution and consume less time. The results obtained from orthogonal arrays were then used as the experimental data to predict the operation parameters at discrete levels for RMS. A back-propagation neural network has been used to approximate the feasible domain of constraints. A 0-1 binary pattern has been used in the input-output layers of the neural network; thus, the computational cost of the training of the neural network is small, compared to the evaluation of the constraints. For PEMFC, the results show that the optimal operation parameters are the temperature of 78^{o}C, anode humidification temperature of 72^{o}C, anode flow rate of 296sccm, cathode flow rate of 295sccm, split flow rate of 145sccm, and split point of 44%.

REFERENCES

Buxbaum R. and Lei H. (2003). Power output and load following in a fuel cell fueled by membrane reactor hydrogen. Journal of Power Sources 123, 43-47.

Chang K. Y. (2011). The optimal design for PEMFC modeling based on Taguchi method and genetic algorithm neural networks. International Journal of Hydrogen Energy 36, 13683-13694.

Chang Y. P., Low C. Y. and Wu C. J. (2007). Optimal design of discrete-value passive harmonic filters using sequential neural-network approximation and orthogonal array. IEEE Transactions on Power Delivery 22, 1813-1821.

Chang K. Y., Lin H. J., and Chen P. C. (2009). The optimal performance estimation for an unknown PEMFC based on the Taguchi method and a generic numerical PEMFC model. International Journal of Hydrogen Energy 34, 1990-1998.

Chang K. Y. and Teng Y. W. (2012). The optimal design for PEMFC modeling based on BPNN and Taguchi method. International Journal of Green Energy 9, 139-159.

Chang Y. P., Chiang M. S. and Wang D. A. (2014). Optimal design of operation parameters on the performance of proton exchange membrane fuel cells using response surface methodology. Journal of Technology 29,161-171.

Cho Y. H., Yoo S. J., Cho Y. H., Park H. S., Park I. S., Lee J. K. and Sung Y. E. (2008). Enhanced performance and improved interfacial properties of polymer electrolyte membrane fuel cells fabricated using sputter-deposited Pt thin layers. Electrochimica Acta 53, 6111-6116.

Hattia M., Meharrarb A. and Tioursic M (2011). Power management strategy in the alternative energy photovoltaic/PEM fuel cell hybrid system. Renewable and Sustainable Energy Reviews 15, 5104-5110.

Ibrahim, A., G. Karimi, K. Jiao and X. Li (2012). Measurement of current distribution in a proton exchange membrane fuel cell with various flow arrangement-A parametric study. Applied Energy 93, 80-89.

Janssen G. J. M. and Overvelde L. J. (2001). Water transport in the porton exchange membrane fuel cell measurement of the effective drag coefficient. Journal of Power Sources 101, 117-125.

Lee Seong Kon, Mogi Gento, Li Zhuolin, Hui K. S., Lee Sang Kon, Hui K. N., Park Sang Yong, Ha Young Jin and Kim Jong Wook (2011). Measuring the relative efficiency of hydrogen energy technologies for implementing the hydrogen economy: An integrated fuzzy AHP/DEA approach. Journal of Hydrogen Energy 36, 12655-12663.

Dong'an Liua, Xinmin Laia, Jun Nib, Linfa Penga, Shuhuai Lana, Zhongqin Lina (2007). Robust design of assembly parameters on membrane electrode assembly pressure distribution. Journal of Power Sources 172, 760-767.

Li Qi, Chen Weirong, Wang Youyi, Liu Shukui and Jia Junbo. (2011). Parameter identification for PEM fuel-cell mechanism model based on effective informed adaptive particle swarm optimization. IEEE Transactions on Industrial Electronics 58, 2410-2419.

Low, C. Y., Chang Y. P. and Hung S. Y. (2009). An application of artificial neural network for sitting and sizing passive harmonic filters. Expert

DOI: 10.6119/JMST-016-0115-2

Systems with Applications 36, 2910-2920.
Rodatz P., Büchi F., Onder C. and Guzzela L. (2004). Uniformity analysis at MEA and stack levels for a Nexa PEM fuel cell system. Journal of Power Sources 128, 231-238.
Tsain J. T. (2012). An evolutionary approach for worst-case tolerance design. Engineering Applications of Artificial Intelligence 25, 917-925.
Yoon Y. G., Lee W. Y., Yang T. H., Park G. G. and Kim C. S. (2003). Current distribution in a single cell of PEMFC. Journal of Power Sources 118, 193-199.